Earth Systems and Environment
https://doi.org/10.1007/s41748-026-01121-7

ORIGINAL ARTICLE

A Novel Cost-Effective Approach for Collecting Time-Series of Turbulence Properties in Aquatic Systems – Part II

Fahad Al Senafi[1] · **Ayal Anis**[2] · **Sebastiano Piccolroaz**[3] · **Tariq Al Rushaid**[1]

Received: 15 November 2025 / Revised: 19 February 2026 / Accepted: 3 March 2026

Abstract

This study presents a novel, cost-effective approach for estimating turbulent kinetic energy dissipation rates (ϵ) and temperature variance dissipation rates (χ_T) using high-resolution data from fast-response temperature sensors. By leveraging a purpose-built MATLAB toolbox (*Solo_T*), we developed an integrated methodology to process temperature time-series, estimate key turbulence parameters, and evaluate mixing processes. The efficacy of this approach is demonstrated through field deployments in the northern Arabian Gulf, a dynamically forced, shallow marine environment influenced by episodic Shamal winds and internal wave activity. The methodology captures key turbulence features and temporal variability under varying atmospheric and oceanographic conditions. A comprehensive description of the toolbox architecture, spectral processing workflow, and the theoretical formulations underpinning the computations is provided. Comparisons with two benchmark microstructure profilers show strong agreement, with discrepancies in ϵ and χ_T estimates within 18%, and correlation coefficients for ϵ ranging between 0.49 and 0.66 across depths, underscoring the accuracy and robustness of the method. This work contributes a reproducible, scalable framework for turbulence studies and expands observational capabilities in coastal, semi-enclosed, and other under sampled aquatic systems, where traditional turbulence profilers are often impractical or cost prohibitive.

✉ Fahad Al Senafi
fahad.alsenafi@ku.edu.kw

[1] Department of Marine Science, College of Science, Kuwait University, Kuwait City, Kuwait

[2] Department of Oceanography, Texas A&M University, College Station, TX, USA

[3] Department of Civil, Environmental and Mechanical Engineering, University of Trento, Trento, Italy

Graphical Abstract

Graphical abstract descriptions: this visual summary serves as a pivotal entry point into the research, offering a concise overview of the study's core findings and methodologies. Comprising simple, clear visuals—such as diagrams, illustrations, and conceptual overlays—it effectively communicates complex data in an accessible format. Logical flow is essential in guiding the reader through the interconnected components of the study, while consistency in color, layout, and typography ensures clarity and visual coherence. High-quality imagery enhances engagement, allowing readers to grasp essential information rapidly and encouraging them to explore the full manuscript. In this graphical abstract, three integrated visual elements convey the scope and significance of the work. The left panel incorporates code fragments and spectral-analysis concepts from the *SOLO_T* MATLAB toolbox, representing the computational engine used to extract ε and χ_t from high-resolution thermistor data. The center panel features satellite imagery of the northern Arabian Gulf, grounding the research in its real observational setting and highlighting the dynamic coastal environment where the methodology was validated. The right panel displays deployment schematics of the custom thermistor frame, emphasizing the cost-effective, field-ready instrumentation central to this study. Overlaid streamline patterns symbolically represent turbulence and scalar transport, visually linking instrumentation, field observations, and analytical processing. Together, these elements provide a concise yet comprehensive overview of the methodology and its relevance to advancing turbulence research in aquatic systems.

Highlights

- Introduces the *Solo_T* MATLAB toolbox, a cost-effective framework to provide estimates of ϵ and χ_T from high-resolution fast thermistors in lieu of traditional microstructure profilers.
- Demonstrates the method under contrasting forcing regimes in the northern Arabian Gulf, including winter Shamal-driven wind event and summer internal waves.
- Validates *Solo_T* estimates against two traditional microstructure profilers, with ϵ and χ_T discrepancies typically within 2–10% and 11–18%, and ε correlations of 0.49–0.66.

Keywords Air-Sea Interaction · Temperature Variance Dissipation Rates · Turbulent Kinetic Energy Dissipation Rates · *Solo_T* Toolbox · Surface Boundary Layer Turbulence

1 Introduction

Understanding ocean turbulence is critical for interpreting energy transfer (e.g. Wang et al. 2020), nutrient mixing (e.g. Spingys et al. 2021), and ecological dynamics within marine environments (e.g. Tozzi, 2004). Turbulence studies underpin numerous applications, from predicting climate-driven changes in ocean circulation to managing fisheries and coastal ecosystems (e.g. Smith et al. 2014; Bakun et al. 2015). Despite its importance, measuring turbulence remains challenging due to the complexity and high costs associated with traditional turbulence profilers (e.g. Thomson et al. 2015; St. Laurent and Merrifield 2017). Recent studies have explored data-driven and machine-learning approaches for environmental monitoring and pattern recognition (e.g. Alif et al. 2025b; Ghosh et al. 2025); however, such methods are typically developed for classification or diagnostic tasks and do not directly provide physically interpretable turbulence dissipation estimates from in situ scalar measurements. In shallow and semi-enclosed systems, external forcings such as rainfall can further modulate stratification and mixing by altering near-surface buoyancy conditions, as highlighted in recent GIS-based rainfall and flood modeling studies (e.g. Alif et al. 2025a). To address these limitations, this study introduces the *Solo_T* Toolbox, a novel computational framework designed to estimate turbulence parameters, namely turbulent kinetic energy dissipation rates (ϵ) and temperature variance dissipation rates (χ_T), using affordable fast-response temperature sensors.

This study builds upon Part I (Al Senafi et al. 2025), which characterized turbulence dynamics in the northern Arabian Gulf under contrasting atmospheric forcing regimes using traditional microstructure profilers. While Part I established the physical processes governing mixing in this region, it also highlighted the operational challenges and costs of sustained turbulence profiling. The present work addresses these limitations by extending the observational framework of Part I through the *Solo*_T Toolbox, enabling continuous turbulence estimates from cost-effective temperature sensors and facilitating longer deployments and broader spatial coverage.

Ocean turbulence research often relies on high-resolution measurements from specialized instruments such as shear probes and velocity profilers (e.g., Anis and Singhal 2006; Mercier et al. 2021; Piccolroaz et al. 2021). These instruments, while effective, are expensive and logistically challenging to deploy in remote or resource-constrained regions over long durations. The Solo_T Toolbox offers an alternative approach by leveraging fast-response temperature measurements to estimate turbulence properties, reducing costs and increasing accessibility while maintaining scientific rigor. This framework is particularly suited for semi-enclosed and coastal seas, where stratification and thermal gradients play a dominant role in mixing processes.

The aim of this study is to introduce the *Solo_T* Toolbox with a validated example of temperature time-series data collected in the unique and fragile marine ecosystem of the northern Arabian Gulf (Fieseler et al. 2023). This region is characterized by complex hydrodynamic processes (Al Senafi & Anis, 2020a; Li et al. 2020b; Bruciaferri et al. 2022) influenced by atmospheric forcing such as Shamal winds (Li et al. 2020a). Through this validation, we demonstrate the toolbox's capability to produce reliable turbulence estimates and its adaptability to various marine environments. The study also seeks to provide a comprehensive overview of the mathematical foundations and computational algorithms underpinning the toolbox, ensuring its utility for the broader oceanographic community.

The specific objectives of this study are to introduce the *Solo_T* Toolbox and document its theoretical foundations, computational algorithms, and spectral processing workflow; to validate estimates of ϵ and χ_T against benchmark microstructure profilers under contrasting forcing regimes, including wind-driven, buoyancy-driven, and internal wave–driven conditions; to demonstrate the toolbox's ability to resolve temporal variability in turbulence across multiple depths and environmental conditions; and to provide a reproducible, open-source framework to support long-duration turbulence observations in coastal and semi-enclosed aquatic systems.

In addition to introducing a cost-effective solution for turbulence measurement, this study contributes to advancing our understanding of the physical processes governing mixing. The insights gained have implications for regional climate studies, ecological modeling, and marine resource management. By bridging the gap between theory and application, the *Solo_T* Toolbox can provide an alternative to how turbulence research might be conducted in diverse marine settings.

2 Methodology

Temperature data were acquired using compact RBR*solo*^{3} T (Temperature) and RBR*duet*^{3} T.D (Temperature & Depth) loggers (RBR Ltd.; see Sect. 2.1) during two field campaigns conducted in distinct environmental conditions and seasons: (1) an internal wave driven regime during summer 2017 (described in 2.2); (2) a wind- and buoyancy-driven environment during winter 2023 (described in 2.3). These deployments provided an opportunity to test and validate the methodology in two contrasting oceanographic settings, which further strengthens the applicability of the method across a range of dynamic oceanographic and meteorological conditions.

2.1 Temperature Loggers, Deployment Setup, and Theoretical Approach

The RBR*solo*^{3} T and RBR*duet*^{3} T.D loggers were chosen due to their cost-effectiveness, portability (~240 mm in length, ~25 mm in diameter), lightweight design (120 g in air, 20 g in water), and high-performance specifications. They offer sampling rates of 2 Hz for standard models and 16 Hz for fast models, with a precision of ±0.002 °C and a resolution better than 0.00005 °C. The fast-response thermistors exhibit a time constant of approximately 70 ms, while the standard models have a time constant of 700 ms. These response times, defined as the duration to reach 63% of the final value (e-folding time; Emery and Thomson 2004), make the sensors ideal for capturing rapid temperature variations linked to turbulent processes. The thermistors' transfer function is characterized as a single-pole system, attenuating higher-frequency signals at a rate of 20 dB per decade. This design allows the RBR*solo*^{3} T sensors to effectively capture rapid temperature variations associated with turbulence, despite some attenuation at higher frequencies. (Gregg and Meagher 1980; Nash et al. 1999; Tagawa et al. 2003).

The fast-response loggers were mounted on custom Delrin frames fabricated in our laboratory (Figs. 1 and 2). This frame featured a rudder (Fig. 1a) connected to the sensor housing (Fig. 1b) via a freely rotating plastic rod-shaft collar (Fig. 1c and d), allowing the assembly to align so that the sensor tip will point into the flow to minimize possible disturbances. The rod was threaded through the mooring line, securing the sensor in place. To prevent wake generation and potential contamination of temperature measurements, the original plastic sensor guards of the temperature sensors were removed (Fig. 2). Additionally, two headless plastic screws were inserted near the sensor head to reduce instrument vibrations (Fig. 1g). The frame was treated with antifouling paint and the exposed part of the logger body was

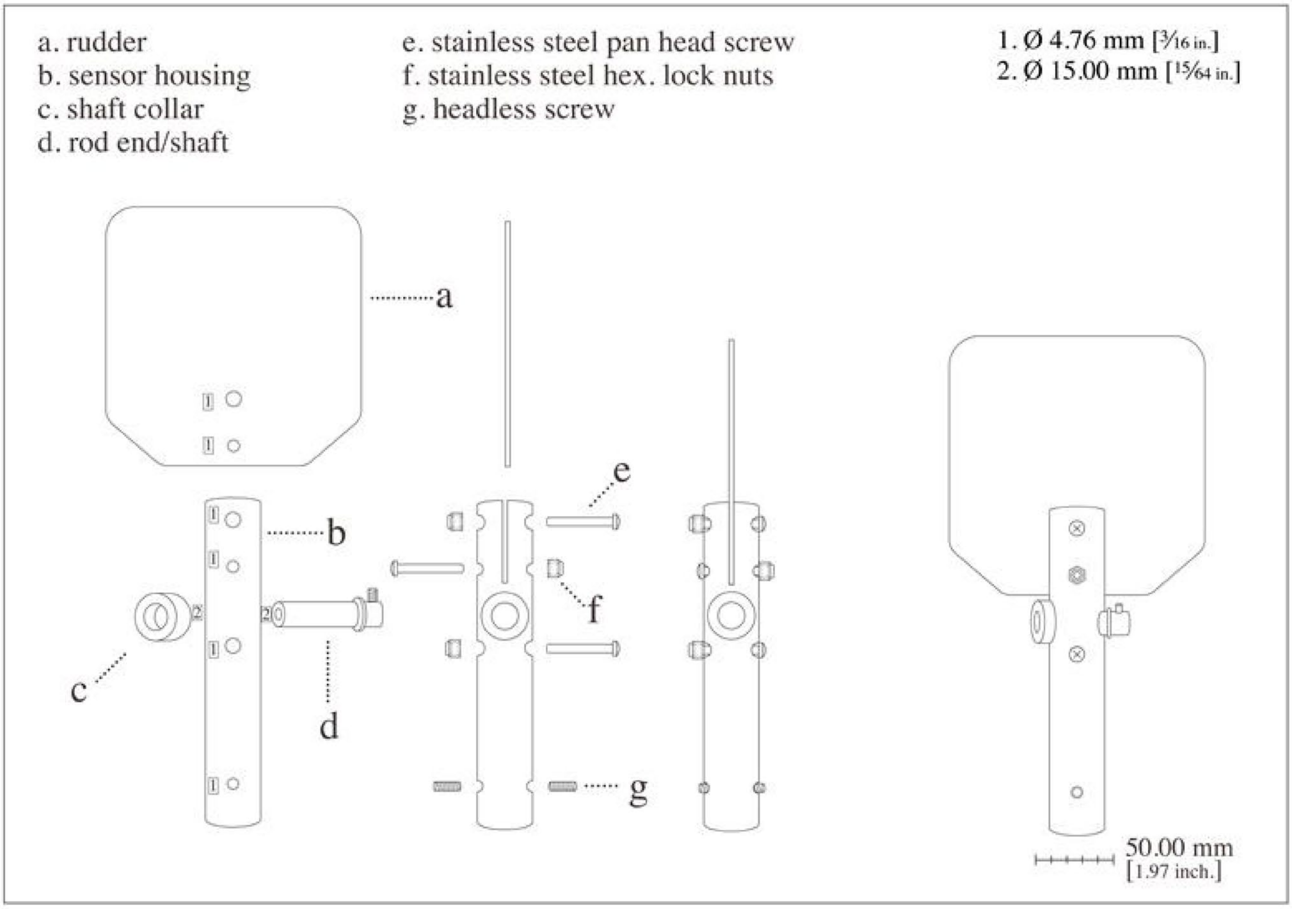

Fig. 1 Assembly diagram of the Delrin frame illustrating key components and hardware. (**a**) Rudder to point in flow direction, (**b**) sensor housing, (**c-d**) shaft rod and collar for mechanical coupling, allowing free rotation, (**e-f**) stainless steel hardware connecting the housing to the wings, (**g**) plastic headless screws designed to minimize sensor vibration. Dimensions are provided in millimeters, with inches indicated in parentheses

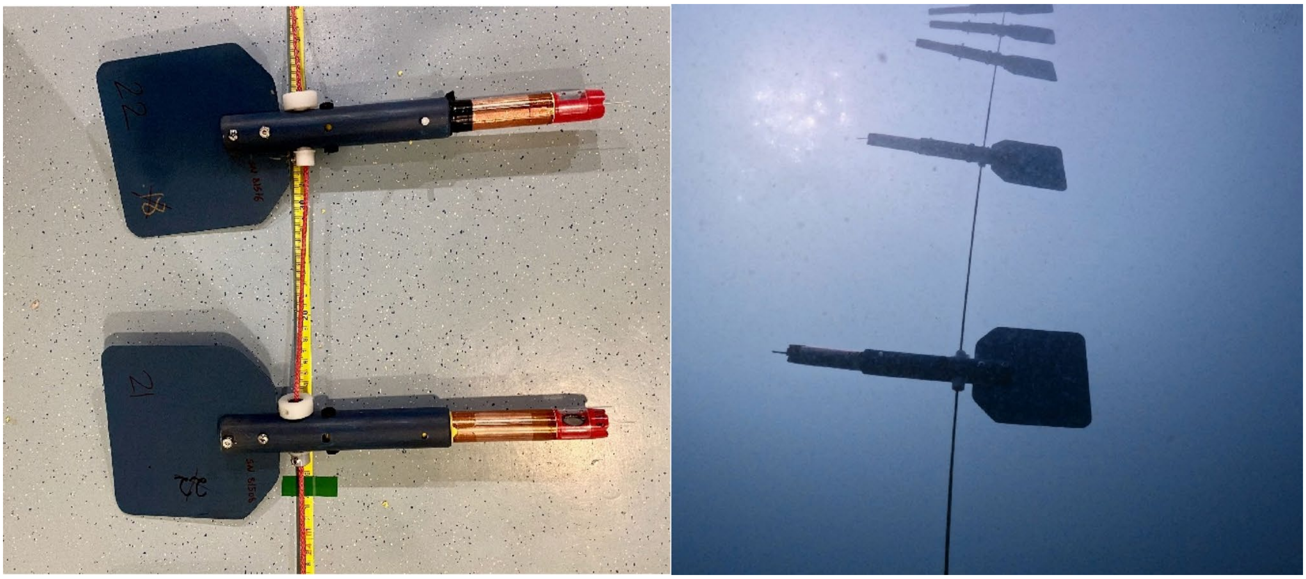

Fig. 2 Photographs of the fully assembled setup: ready for deployment (left) and during measurements in the Arabian Gulf (right)

covered with a thin copper foil to ensure high-quality data during long-term deployments, a configuration that proved effective over the deployment period, with no evidence of biofouling despite the region being heavily impacted by biofouling. All loggers were recalibrated by the manufacturer prior to deployment to maintain measurement accuracy.

Estimation of turbulence parameters in the *Solo_T* Toolbox begins with the fundamental definitions of ϵ and χ_T. These parameters describe the rate at which energy cascades from large to smaller scales and the dissipation of temperature variance, respectively (e.g. Hill 1978; Kerr 1990; Sreenivasan 1996; Kundu and Cohen 2012; Portwood et al. 2022). Temperature fluctuations in a turbulent field adhere to scalar turbulence theory, where the power spectral density (PSD) of temperature gradients follows a characteristic−5/3 slope within the inertial-convective subrange. This theoretical framework provides the foundation for estimating the dissipation of temperature variance, expressed as:

$$\chi_T = 2D\langle(\nabla T')^2\rangle \tag{1}$$

where T' denotes the fluctuating component of temperature, $\nabla T'$ represents its spatial gradient, and D is the molecular diffusivity of heat. The operator $\langle\cdot\rangle$ computes the mean of the enclosed quantity, making $\langle(\nabla T')^2\rangle$ the mean-square value (or variance) of the temperature gradient. This variance provides a direct measure of the intensity of small-scale temperature fluctuations. For isotropic turbulence, this can be simplified along the longitudinal direction, x, as:

$$\chi_T = 6D\langle\left(\frac{\partial T'}{\partial x}\right)^2\rangle \tag{2}$$

To enable the use of theoretical turbulence models, Taylor's frozen flow hypothesis (Taylor 1938) is assumed to convert time-domain into cyclic longitudinal wavenumber (k) space, where:

$$k = \frac{2\Pi f}{u} \tag{3}$$

here, f is the frequency, and u is the mean flow speed obtained here from Acoustic Doppler Current Profiler (ADCP) measurements. The conversion from frequency to wavenumber space was performed using Taylor's frozen turbulence hypothesis, which assumes that turbulent structures are advected past the sensor by the mean flow with negligible temporal evolution. This approximation is appropriate when the mean advective velocity substantially exceeds turbulent fluctuation velocities. Mean flow speeds were obtained from co-located ADCP measurements for each analysis segment. No explicit minimum flow-speed threshold was imposed; instead, the applicability of Taylor's hypothesis was enforced through objective spectral quality-control criteria, whereby only segments exhibiting a resolved inertial–convective subrange, a consistent−5/3 slope, and spectral levels exceeding the noise floor in wavenumber space were retained (Taylor 1938; Wilczek et al. 2014). This conversion allows the computation of χ_T in wavenumber space as:

$$\chi_T = 6D\int_0^\infty \Phi_{T'x}(k)\,dk \tag{4}$$

where $\Phi_{T\prime_x}$ represents the PSD of the longitudinal temperature gradient, $T_x' = \partial T\prime/\partial x = (1/u)\,(\partial T\prime/\partial t)$. We note that no explicit minimum flow-speed threshold was imposed; instead, the applicability of Taylor's hypothesis is assessed implicitly through spectral quality-control requirements. Periods of very weak flow therefore tend to be excluded indirectly, as they do not satisfy the objective fit-quality criteria used to retain spectra in the inertial–convective range.

Further physical properties, such as the vertical eddy diffusivity for heat (K_T) can be estimated to quantify heat transport within the water column. The vertical eddy diffusivity, K_T, as described by Osborn and Cox (1972), is given by:

$$K_T = \frac{\chi_T}{2T_z^2} \tag{5}$$

where T_Z is the mean vertical temperature gradient.

In steady-state conditions, where the dissipation of turbulent kinetic energy is balanced by mechanical shear production and buoyancy production, the eddy diffusivity for density, K_ρ, can also be estimated. As described by Osborn (1980), K_ρ is given by:

$$K_\rho = \frac{\Gamma\epsilon}{N^2} \tag{6}$$

where, Γ is the mixing efficiency and N is the buoyancy frequency. Because the moored temperature sensors did not include conductivity measurements, N^2 was estimated from vertical temperature gradients under the assumption of vertically uniform salinity. This approximation is supported by concurrent MicroCTD profiles, which indicated weak vertical salinity variability and a comparatively minor haline contribution to density stratification during the deployment period. A constant mixing efficiency Γ =0.2 was adopted following Osborn (1980) for statistically steady, shear-driven stratified turbulence. Because $\epsilon \propto \Gamma^{-3/2}$, varying Γ between 0.1 and 0.3 (Ivey et al. 2008) changes ϵ by factors of 2.83 and 0.54, respectively, relative to Γ =0.2. These variations fall within the uncertainty typically associated with microstructure-based dissipation estimates (e.g., Oakey 1982).

Assuming $K_T = K_\rho$ following the Osborn–Cox framework, which is appropriate when temperature behaves as a passive scalar under approximately steady, shear-driven stratified turbulence, and noting that departures from this assumption are generally limited to order-unity differences outside strongly double-diffusive or highly nonstationary regimes, an expression for ϵ can be derived as follows:

$$\epsilon = \frac{N^2\chi_T}{2\Gamma T_z^2}. \tag{7}$$

The mean-square turbulence temperature fluctuations, also referred to as variance, in the longitudinal x -direction, are given by:

$$\langle T\prime^2\rangle = \int_0^\infty \Phi_{T\prime}(k)\,dk \tag{8}$$

where, $\varphi_{T\prime}$ is the one-dimensional spectral density of the temperature fluctuations. Within the inertial-convective range, dimensional analysis (e.g. Sreenivasan 1996; Danaila and Antonia 2009) links $\Phi_{T\prime}(k)$ to the wavenumber as:

$$\Phi_{T\prime}(k) = C_{OC}\epsilon^{-1/3}\chi_T k^{-5/3} \tag{9}$$

Here, $C_{oc} = 0.4$ is the Obukhov-Corrsin constant (Sreenivasan 1995). When temperature fluctuation measurements produce well-resolved spectra in the inertial-convective range, the spectra are expected to exhibit a -5/3 slope in log-log space. Normalizing the spectra using $C_{oc}k^{-5/3}$ results in:

$$\frac{\Phi_{T\prime}(k)}{C_{OC}k^{-5/3}} = \epsilon^{-1/3}\chi_T \tag{10}$$

where the right-hand side combines the turbulent kinetic energy dissipation rate and temperature variance dissipation rate within the inertial-convective range. Rearranging Eq. (7) yields another relationship between ϵ and χ_T:

$$\frac{N^2}{2\Gamma T_z^2} = \epsilon\chi_T^{-1}. \tag{11}$$

From Eqs. (10) and (11), ϵ and χ_T can be computed resulting in:

$$\epsilon = \left(\frac{N^2\Phi_{T\prime}(k)}{2\Gamma C_{OC}T_z^2k^{-5/3}}\right)^{3/2} = \left(\frac{6.25N^2\Phi_{T\prime}(k)}{T_z^2k^{-5/3}}\right)^{3/2} \tag{12}$$

$$\chi_T = \left(\frac{N^2\Phi_{T\prime}^3(k)}{2\Gamma C_{OC}^3k^{-5}T_z^2}\right)^{1/2} = \left(\frac{39.0625N^2\Phi_{T\prime}^3(k)}{T_z^2k^{-5}}\right)^{1/2}. \tag{13}$$

where the numerical factor 6.25 results from the values of $\Gamma = 0.2$ and $C_{OC} = 0.4$.

Temperature time-series were collected from thermistor strings with each string including several thermistors at different depths (see Fig. 2). The data was used to compute stratification parameters N^2 and T_z^2, as well as to derive $\Phi_{T\prime}^3$ at the respective thermistors depths. Estimates of ϵ and

χ_T were then made at the respective thermistor depths using Eqs. (12) and (13).

2.2 Internal Wave Driven Conditions (Summer 2017)

A two-week dataset collected during the July 2017 field campaign provided a comprehensive time-series of internal wave dynamics driven by semidiurnal tides and turbulence measurements in the northern Arabian Gulf (see Al Senafi and Anis 2020b; 2020c for detailed descriptions). Specifically, the M3 mooring, deployed 1.65 km off the coast of Kuwait at a depth of ~ 14 m, recorded temperature fluctuations using five RBR*solo*^{3} T loggers sampling at 2 Hz, positioned at 2.5, 5.0, 7.5, 9.5, and 11.5 m above bottom (MAB). Additionally, an upward-looking 2 MHz Nortek ADCP captured current velocity profiles at 15 s intervals. Data from these five loggers and ADCP are provided in the *Solo_T* Toolbox as an example. Benchmark turbulence estimates were derived from two different microstructure profilers: a Rockland Scientific International Inc. (RSI) MicroCTD and a Precision Measurement Engineering (PME) Self-Contained Autonomous Microstructure Profiler (SCAMP, described in 2.4).

2.3 Wind and Buoyancy Driven Environment (Winter 2023)

The one-month dataset collected during the November 2023 field campaign provided a high-resolution time-series of wind-driven and buoyancy-driven turbulence in the northern Arabian Gulf. The study site was located near Qarooh Island, Kuwait, 44 km east of the Kuwaiti mainland and 120 km south of the Euphrates-Tigris delta, at a depth of 30.4 m. This site was chosen for its deep, open-water conditions, minimizing obstructions to the dominant northwesterly Shamal and southeasterly Kaus winds, the primary atmospheric forcings examined in that study (see Al Senafi et al. 2025 for detailed field descriptions).

To investigate the thermal and turbulence structure of the water column, a moored array of 22 compact RBR*solo*^{3} T and RBR*duet*^{3} T.D loggers was deployed along a tight mooring line. These sensors recorded temperature fluctuations at up to 16 Hz, with vertical spacing ranging from 0.25 m near the surface and bottom boundary layers to 4 m in the mid-layer. Additionally, a bottom-mounted 1 MHz Nortek ADCP was deployed 25 m away from the mooring at a depth of 30.4 m, providing continuous current velocity profiles. This dataset captured the transition from calm pre-Shamal conditions to strong, Shamal-induced turbulence, revealing the effects of mechanical, wind-driven, and convective cooling mixing on vertical stratification. To benchmark the turbulence estimates derived from the temperature loggers, an RSI MicroCTD microstructure profiler was used.

2.4 Turbulence Profiling

As mentioned above, a MicroCTD (Rockland Scientific 2022) and a SCAMP (Stevens et al. 1999) microstructure profilers were deployed simultaneously with the moored thermistors strings for benchmarking. Both microstructure profilers are specifically designed for application in shallow aquatic systems, such as coastal areas. In both cases, profiles, spanning the water column from about 1 m below the surface to 0.1 m above the bottom, were collected at a rate of one profile every 4–10 min, depending on the water depth at the sampling station. Data was stored internally and later uploaded to a host laptop PC. In the following, we describe the two profilers and the main post-processing steps for analysis of microstructure data.

Comparisons between moored temperature-based estimates of ϵ and χ_T and estimates derived from the MicroCTD and SCAMP turbulence profilers were performed using synchronized time–depth alignment. Temperature-derived estimates were computed over fixed windows of 1024 samples for standard (2 Hz) sensors and 8192 samples for fast (16 Hz) sensors, corresponding to 8–9 min durations chosen to match the profiler sampling interval. Profiler estimates were vertically averaged at the corresponding sensor depths, and ADCP-derived mean flow speed was interpolated to the midpoint of each segment for use in the frequency–wavenumber transformation. Segments with insufficient spectral resolution or poor signal-to-noise were excluded through the applied spectral quality-control criteria.

2.5 Processing of the RSI MicroCTD Data

The MicroCTD is a 1 m long turbulence profiler equipped with two microstructure airfoil shear probes and two fast response temperature sensors (type FP07) sampling at high frequency (512 Hz). The airfoils are positioned orthogonally to each other to measure both components of the horizontal velocity shear fluctuations $\partial u\prime/\partial z$ and $\partial v'/\partial z$, where the indicates turbulent fluctuations. A pair of piezo-accelerometers is installed inside the instrument, sampling at 512 Hz, and are used to assist on removing possible contamination of the shear probes signal due to vehicle vibrations. The instrument is also equipped with a pressure transducer and a precision conductivity-temperature sensor, both sampling at 64 Hz.

The turbulence data were processed using scripts included in RSI's ODAS libraries (v4.4), modified according to the procedure described in Piccolroaz et al. (2021).

The raw shear and FP07 signal were converted into physical units using the calibration sensitivities of the shear probes and using the precision temperature sensor as benchmark, respectively. Each vertical profile was divided into 2 m segments. Each segment included 1024 samples (2 s bins) with 512 sample overlap (50%). Spectra of velocity shear and temperature gradient were calculated for each 2 m segment by averaging results from five 50% overlapping, detrended and Hanning tapered sub-segments. This provided a smoothed representation of the turbulence structure in each 2 m segment. Frequency spectra were converted to the corresponding wavenumber spectra using Taylor's frozen turbulence hypothesis (Eq. 3) using the profiler free fall speed (w) obtained differentiating the pressure time series. Before calculating the shear spectra, the signal was cleaned by removing spikes and high-pass filtered to remove noise originating from the low-frequency motions of the free-falling profiler. The shear spectra were then corrected for the spatial response of the probe and for contamination from higher frequency noise using the data from the piezoelectric accelerometers of the instrument. Similarly, temperature gradient spectra were corrected for the frequency response of the probes using a single pole transfer function, accounting for the sensor-dependent time constant (7 ms; FP07).

The shear and temperature gradient wavenumber spectra obtained were subsequently used to estimate vertical profiles of ϵ and χ_T. Specifically, ϵ was evaluated under the assumption of small-scale isotropy as:

$$\epsilon = \frac{15}{2}\nu\langle\left(\frac{\partial u'}{\partial z}\right)^2\rangle = \frac{15}{2}\nu\int_0^\infty \psi_{u'_z}(k)\,dk, \tag{14}$$

where ν is the kinematic viscosity of water, the term $\langle\left(\frac{\partial u'}{\partial z}\right)^2\rangle$ is the variance of the velocity shear fluctuations, and $\psi_{u'_z}$ is the shear wavenumber spectrum associated with the vertical gradient of the horizontal velocity fluctuations u'. Solving the integral on the right-hand side of Eq. (14) over the resolved wavenumber range $[k_L, k_U]$, where k_L and k_U represent the lower and upper bounds of the resolved spectral range, provides a first estimate of ϵ. This estimate was successively adjusted accounting for the unresolved fraction of the variance using the empirical Nasmyth spectrum according to the procedure delineated in Piccolroaz et al. (2021).

χ_T was evaluated following Eq. 1 to 4. The maximum likelihood estimation method proposed by Ruddick et al. (2000) was used to fit the Kraichnan theoretical spectrum to the measured spectrum, to estimate χ_T and an additional value of ϵ. The agreement between observed spectra and reference spectra (Nasmyth spectrum for shear; Kraichnan spectrum for temperature gradients) was quantified using the Mean Absolute Deviation (MAD) computed over the integration band. A segment was rejected if $MAD > MAD_c = 2(2/d)^{0.5}$, where d is the number of degrees of freedom of the spectral estimate. The number of degrees of freedom depends on spectral technique, window, and averaging methods, and can be quantified as $d = 1.9N_{fft}$, where N_{fft} is the total number of fast Fourier transform segments. In our case, spectra were calculated considering five 50% overlapping, detrended and Hanning tapered sub-segments, which gives $d = 9.5$. We refer the reader to Piccolroaz et al. (2021) for the definition of MAD.

As for the temperature gradient spectra, additional quality metrics were used. First, only segments with a signal to noise ration (SNR) larger than 1.3 over the selected integration band were accepted. This threshold ensures that the measured spectrum significantly exceeds the instrumental noise level. Then, the likelihood of the Kraichnan spectral fit was compared to that of a power-law fit. Only fits with a likelihood ratio between the two larger than 10^2 were accepted, ensuring that measured spectrum did resolve the change of slope between the viscous-convective and viscous diffusive subrange. Also, to ensure that the fitted temperature spectrum included both the spectral peak and the initial roll-off region, segments were accepted only $k_L < k_P$, $\log_{10}(k_U) - \log_{10}(k_L) > 0.8$, and $k_U > 2k_P$, where k_P denotes the spectral peak wavenumber.

We refer the reader to Ruddick et al. (2000) and Piccolroaz et al. (2021) for additional details of the iterative fitting procedure. In these studies, metrics of χ_T and ϵ are provided as well include criteria for the quality of the fit, the signal-to-noise ratio, and the sufficient resolution of the wavenumber range. Poor fits or unresolved ranges were excluded from the analysis to ensure the robustness of the χ_T and ϵ estimates.

2.6 Processing of the PME SCAMP Data

Similar to the MicroCTD, the SCAMP is a battery powered, portable, lightweight (6 kg, 0.76 m length) profiler that measures temperature, conductivity, temperature-gradient microstructure, and pressure while free falling at a nominal speed of 0.1 m/s. SCAMP's sensors included two FP07 fast-response (time constant ~ 7 ms) thermistors, separated by about 3 mm; a more accurate and stable but slower temperature (T1201 thermistor, time constant ~ 200 ms) and conductivity (PME 4-electrode ceramic, spatial resolution ~ 1 cm) sensor pair located ~ 5 cm beneath the fast response sensors; and a pressure sensor (Keller PSI PAA-10). SCAMP's sampling rate is 100 Hz and allows measurement of scales as small as ~1 mm.

χ_T was estimated by direct integration of SCAMP's microstructure temperature-gradient spectra (e.g. Oakey

1982) of linearly-detrended segments of 1024 points (~ 1.0 m bins in the vertical), using the Welch method with a 512-point Hanning window with 50% overlap (e.g. Press et al. 1992), after allowance for instrument noise. ϵ was estimated by fitting the observed microstructure temperature-gradient spectra to both the theoretical Batchelor spectrum (Batchelor 1959; Oakey 1982) as well as to the theoretical Kraichnan spectrum (Kraichnan 1968) using the same maximum likelihood estimation method (Ruddick et al. 2000) used also for the processing of the MicroCTD data. We note that both the Batchelor and Kraichnan spectral models resulted in estimates generally within a few percents of each other. Similar metrics as those used for evaluating the MicroCTD measurements were used to assess the quality of the estimates for χ_T and ϵ.

3 *SOLO_T* Toolbox Design and Data Structure

The *SOLO_T* Toolbox is a MATLAB-based software suite designed to compute turbulence properties such as ϵ and χ_T from high-resolution temperature time-series data. The toolbox uses computational methods, robust noise modeling, and theoretical spectral fitting techniques to provide reliable turbulence estimates from data collected using RBR*solo*³ T sensors or similar thermistors. This section details the design, workflow, and computational processes implemented in the toolbox.

The toolbox is organized into five primary directories to streamline user interaction and computational workflows. The example data folder contains sample datasets from the 2017 Kuwait field campaign (see Sect. 2.2 for details) and includes output figures for each function, enabling users to validate the toolbox's functionality. The *five3rd* directory focuses on spectral fitting to the inertial-convective subrange, allowing calculations of ϵ and χ_T based on fitting of the PSD to the −5/3 slope. Advanced computational algorithms required for spectral processing are housed in the *IoSR_Surrey_Matlab* Toolbox (Hummersone, 2024), while the *MLE* directory provides tools implementing the Maximum Likelihood Estimation (MLE) method. Auxiliary functions essential for data handling, visualization, and noise modeling are included in the private folder.

The following subsections describe the primary functions within the *SOLO_T* Toolbox, each designed to address specific aspects of high-resolution temperature data analysis, including determining instrument electronic noise levels (Sect. 3.1), data visualization (Sect. 3.2 & 3.3), and advanced processing and spectral analysis to estimate ϵ and χ_T (Sect. 3.4–3.6).

3.1 Function: Solo_T_Noise_spc.m

The function *solo_T_noise_spc* is a diagnostic tool in the *SOLO_T* Toolbox, specifically designed to analyze and quantify noise contributions in high-resolution temperature time-series data collected in lab-controlled conditions, with the thermistor fully enclosed in a tube wrapped with aluminum foil for electromagnetic shielding. Accurate identification and handling of noise are essential for reliable turbulence computations, particularly when estimating key parameters like ϵ and χ_T so that they are not biased by noise contamination.

The primary purpose of *solo_T_noise_spc* is to compute and visualize the PSD of temperature fluctuations and distinguish meaningful signal components from noise. Temperature signals, particularly those at high frequencies, can be contaminated by electronic noise inherent to the sensor's circuitry. This function characterizes the spectral shape of the noise and its level to allow subsequent spectral corrections.

The noise spectrum is modeled as broadband white noise, represented by a flat PSD over a range of frequencies. The PSD of the observed temperature signal ($\Phi(f)$) is computed using Welch's method:

$$\Phi(f) = \left| \sum_{n=1}^{N} \frac{1}{N} T(t)\, e^{-i2\pi f t} \right|^2 \tag{15}$$

where $T(t)$ is the temperature time series and N is the number of points in the segment (Hayes 1996; Oppenheim, 1999; Stoica et al. 2005). The PSD is then analyzed to identify the flat, high-frequency component indicative of sensor noise.

Once the noise level is identified, the function plots the observed PSD alongside the identified noise floor. This allows to visually assess whether the signal-to-noise ratio (SNR) is sufficient for reliable turbulence analysis. Key parameters, such as the white noise level, are estimated by this function. For example, RBR*solo*³ T sensors (2 and 16 Hz) white noise level is typically in the range of 10^{-9} to 10^{-8} °C²/Hz (Fig. 3).

3.2 Function Solo_T_Contours.m

The *solo_T_contours* function is a visualization tool, designed to produce contour plots of temperature time-series. These contour plots allow visualization of the spatial and temporal structure of temperature variations. By presenting the data in a two-dimensional format, patterns, gradients, and zones of enhanced mixing or stratification may be identified (Fig. 4).

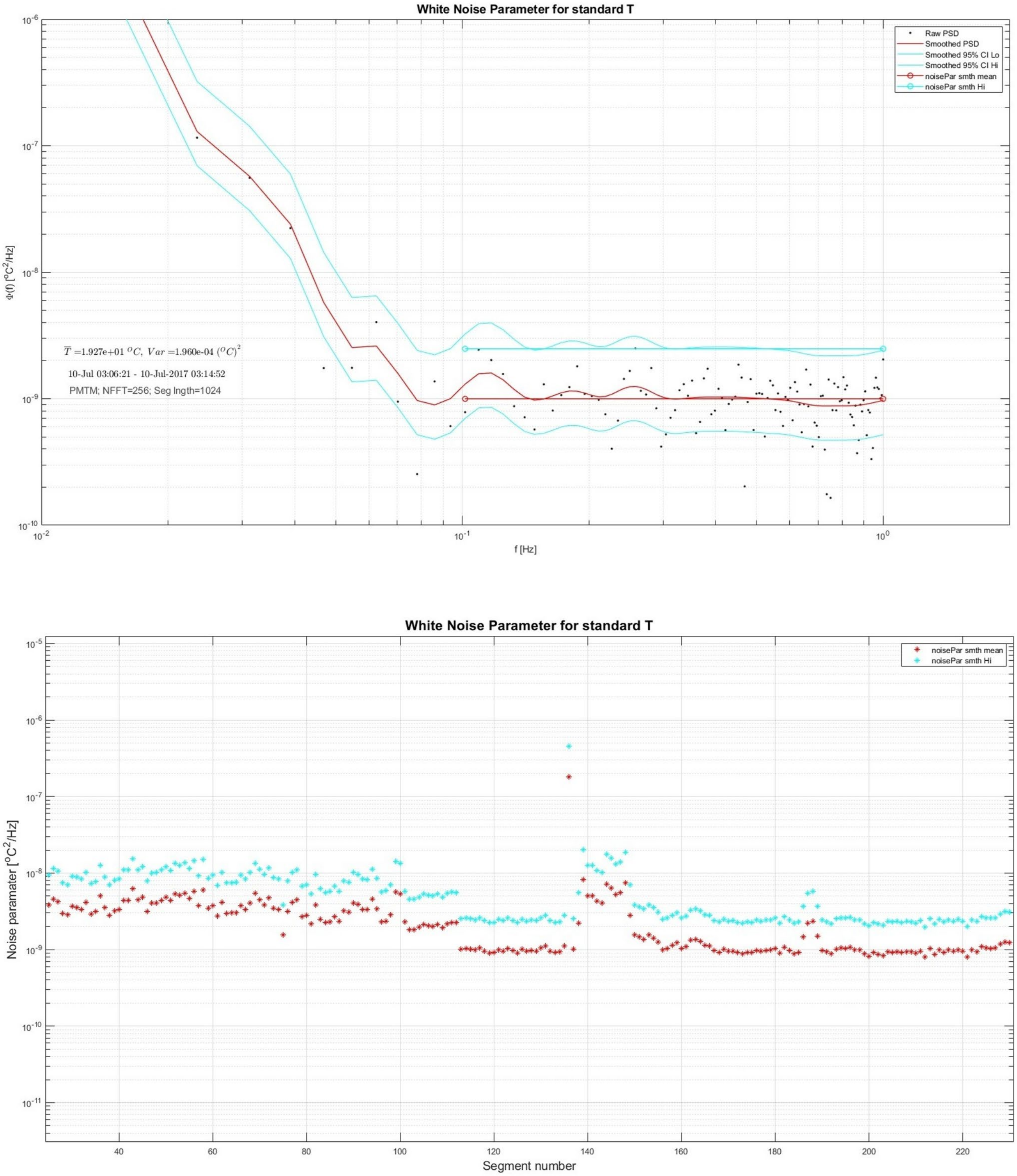

Fig. 3 Analysis of white noise for standard RBR*solo*³ T loggers using *solo_T_noise_spc* function. The top panel displays the PSD of temperature time-series data. The black dots represent the raw PSD, while the red line indicates the smoothed PSD. The cyan lines denote the 95% confidence intervals (CI) of the smoothed PSD. The horizontal cyan circles represent the estimated white noise level, with the mean noise floor shown in red. The bottom panel illustrates the temporal variability of the white noise parameter across data segments

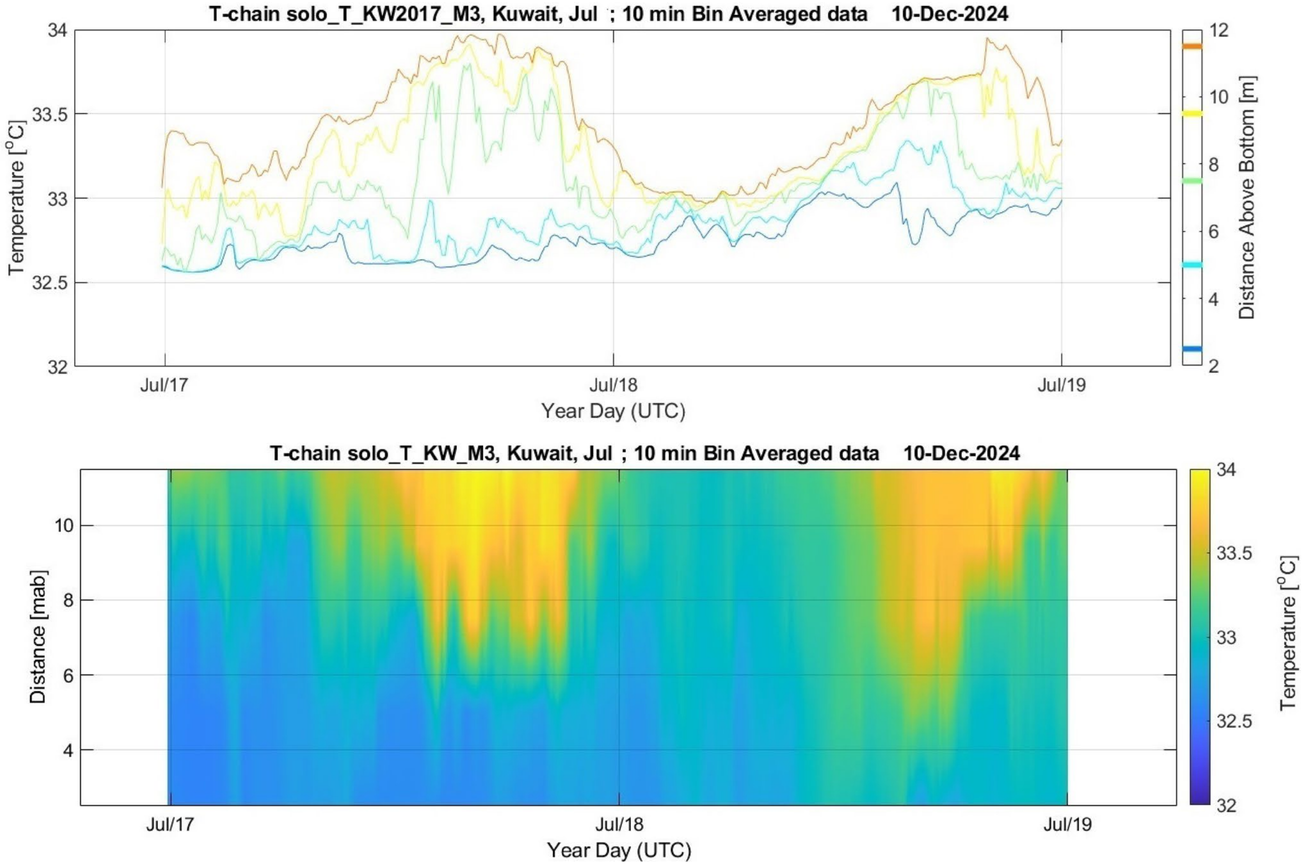

Fig. 4 Visualization of temperature data using the *solo_T_contours* function. The top panel presents temperature traces from multiple sensors deployed along the water column, color-coded by their distance above the seabed. The bottom panel illustrates the same data as a contour plot. Data were bin averaged over 10-minute intervals

This function arranges the temperature data into a matrix, where rows represent different sensor depths, and columns represent time steps. It linearly interpolates the data onto a regular grid to ensure smooth transitions between sensor depths and time intervals. Users have the flexibility to define the interpolation resolution, which can be adjusted based on the temporal and vertical sampling density of the dataset.

3.3 Function: Solo_dTdt_plot.m

The function *solo_dTdt_plot* designed to visualize time derivatives of temperature (dT/dt) from high-resolution temperature measurements. Computing dT/dt is used in turbulence analysis, as it is directly linked to χ_T, a key parameter for understanding heat and scalar transport in marine environments. The function provides a way to analyze and validate dT/dt by generating time-series and fluctuation plots, offering insights into the temporal dynamics of the observed temperature field. This visualization enables to identify regions of high variability, discern flow structures, and detect noise or artifacts in the data, ensuring the integrity of subsequent computations.

Solo_dTdt_plot begins with computing time derivatives of temperature numerically, using finite difference methods (there are different types and edges may be treated different than inside points):

$$\frac{dT}{dt} \approx \frac{T\left(t+\Delta t\right)-T\left(t\right)}{\Delta \mathrm{t}} \tag{16}$$

where $\Delta \mathrm{t}$ the sampling interval. A significant strength of the function lies in its ability to generate clear and detailed visualizations of dT/dt. The time-series plots highlight key features such as turbulent bursts, while color gradients and markers enhance the interpretability of the data (Fig. 5). These visualizations serve not only as diagnostic tools for assessing noise or anomalies in the temperature data but also as a means of validating the suitability of the data for further turbulence analysis.

3.4 Function Solo_T_Spectrogram.m

The *solo_T_spectrogram* function computes and displays a spectrogram of temperature fluctuations. A spectrogram

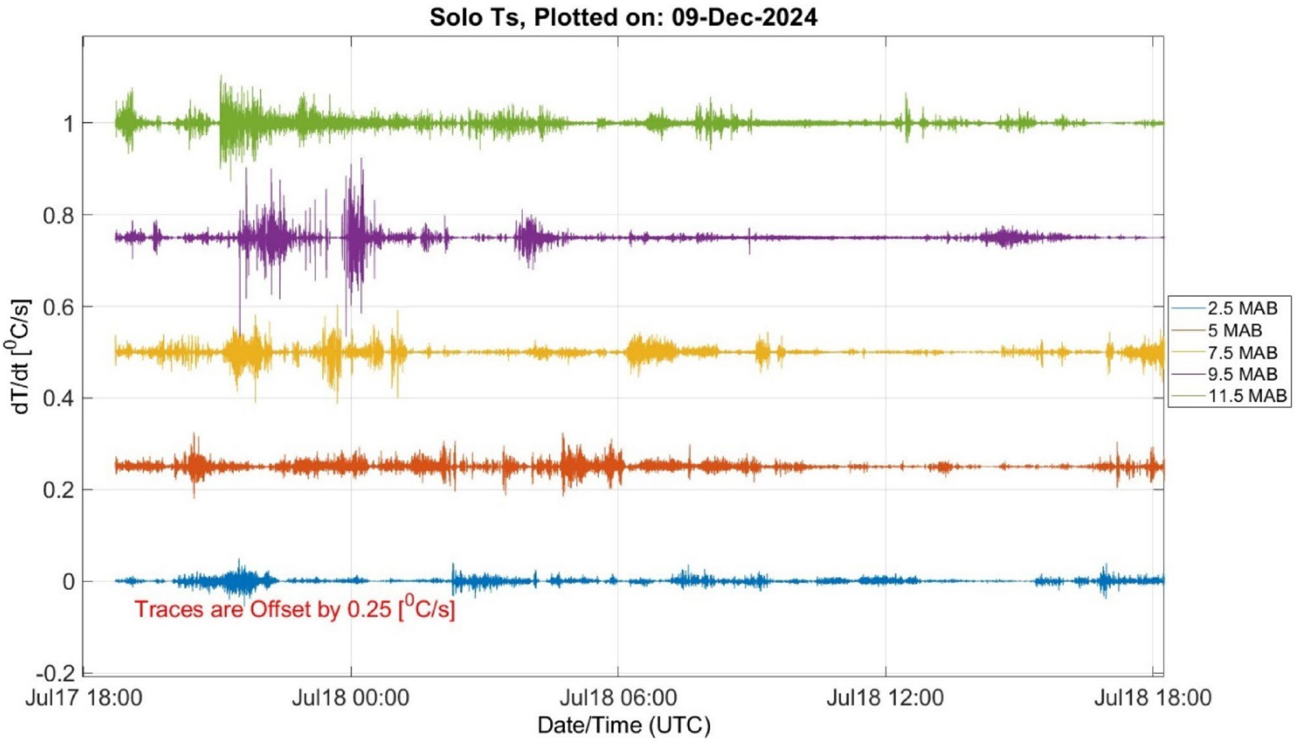

Fig. 5 Visualization of temperature rate-of-change (dT/dt) using the *solo_dTdt_plot* function. The figure presents the temporal variation of dT/dt (°C/s) measured at five distinct heights above the seabed (labeled as 2.5 MAB, 5 MAB, 7.5 MAB, 9.5 MAB, and 11.5 MAB). Each trace is color-coded and offset by 0.25 °C/s for clarity

provides a visual representation of how the PSD of temperature fluctuations varies over time, offering insights into the temporal evolution of turbulence and mixing processes in the water column.

The primary objective of this function is to analyze the spectral characteristics of temperature data within specific time windows and represent these characteristics as a function of both frequency and time. This dual-domain representation is particularly useful for identifying dynamic changes in turbulence intensity, such as those caused by external forcing events (e.g., winds or tidal influences), and for recognizing temporal patterns in the underlying temperature field.

The function begins by dividing the temperature time series into segments of user-defined length. Each segment is detrended and a Hanning window is then applied to each segment to minimize spectral leakage, ensuring that the resulting PSD is an accurate representation of the energy distribution across frequencies (Welch,1967; Harris 1978; Oppenheim, 1999). The function uses Welch's method to calculate the PSD for each segment, which involves averaging the PSDs of overlapping data windows to reduce noise and enhance spectral resolution. The resulting PSDs are then plotted as a function of frequency and time, creating a spectrogram that captures the time-dependent spectral energy distribution of the temperature field.

One of the key strengths of the *solo_T_spectrogram* function is its ability to reveal dynamic shifts in the temperature spectra. For example, during periods of enhanced turbulence, the spectrogram often shows an increase in spectral energy at higher frequencies, corresponding to smaller spatial scales. This feature helps to correlate observed changes in the spectral energy distribution with external drivers such as wind stress, buoyancy fluxes, or tidal forcing (Fig. 6).

3.5 Function Solo_T_FitPSD_kSpace.m

The *solo_T_FitPSD_kSpace* function is designed to fit observed temperature PSDs to theoretical turbulence models in the wavenumber domain (k-space). The primary goal of this function is to estimate turbulence properties, ϵ and χ_T, using observed PSDs and the theoretical −5/3 approach described in Sect. 2.

After loading the high-resolution temperature time-series data, the function interpolates the velocity data in both time and depth to align with user defined temperature segments. Subsequently, the aligned data are used to compute the temperature PSD for each segment. The PSD is then smoothed using fractional-octave smoothing (1/N-octave smoothing) implemented through the IoSR MATLAB Toolbox (Hummersone, 2024). The function then transforms the temperature data into the wavenumber domain using Taylor's frozen

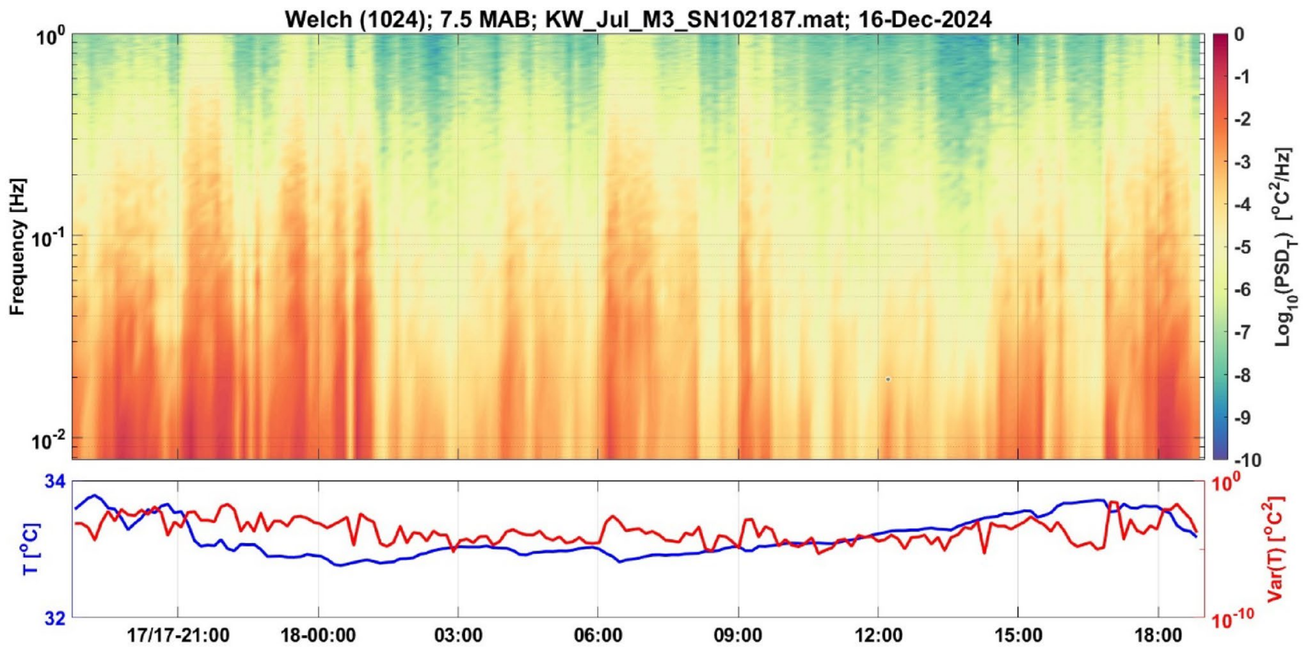

Fig. 6 Spectrogram of temperature time-series data using the *solo_T_spectrogram* function. The top panel illustrates the time-frequency representation of temperature fluctuations at 7.5 MAB, derived from Welch's method with 1024 data points per segment. The color map represents the PSD in units of °C²/Hz, where warmer colors indicate higher power levels. The lower panel displays the corresponding time series of temperature (T, °C) in blue and its variance (Var(T), °C²) in red

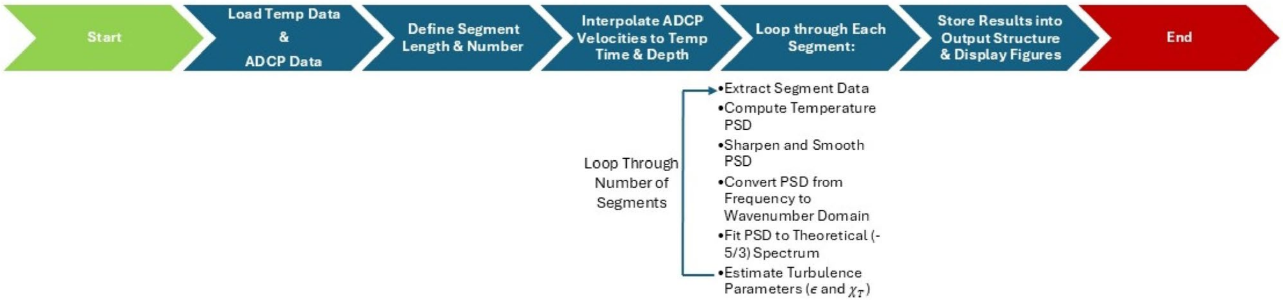

Fig. 7 Flowchart illustrating the computational workflow of the *solo_T_FitPSD_kSpace* function

turbulence hypothesis (Eq. 3) and fits the observed PSD to a theoretical spectrum using the MLE method (Fig. 7). Specifically, it applies both the Batchelor and Kraichnan spectral models for passive scalar turbulence, which describes the energy distribution across wavenumbers and accounts for viscous and diffusive effects at small scales (Batchelor 1959; Kraichnan 1968; Oakey 1982; Ruddick et al. 2000).

This statistical technique evaluates the likelihood of the observed PSD given the theoretical model, iteratively adjusting ϵ and χ_T to maximize this likelihood. The outputs are the best-fit values of ϵ and χ_T, along with the residuals, which quantify the goodness-of-fit. To enhance accuracy, the function preprocesses the data to remove sensor noise by subtracting a noise spectrum, derived from bench tests and use of function *solo_T_noise_spc* (Sect. 3.1). Results are visualized through a comparison of the observed and fitted spectra plotted in log-log space. The function overlays the observed PSD, the theoretical fit, and the residuals, providing an assessment of the goodness of the fit and the validity of the turbulence model (Fig. 8).

3.6 Function Solo_T_Quick_calc.m

The *solo_T_quick_calc* function provides a rapid estimation of turbulence properties, including ϵ and χ_T. It is tailored for quick analysis without the need to plot or to delve into the detailed, step-by-step processes that other functions in the toolbox provide. By automating key tasks, this function allows preliminary results or data validation.

The function begins by loading the temperature data from user-specified input files. Once the data is loaded, the function preprocesses it by performing noise correction

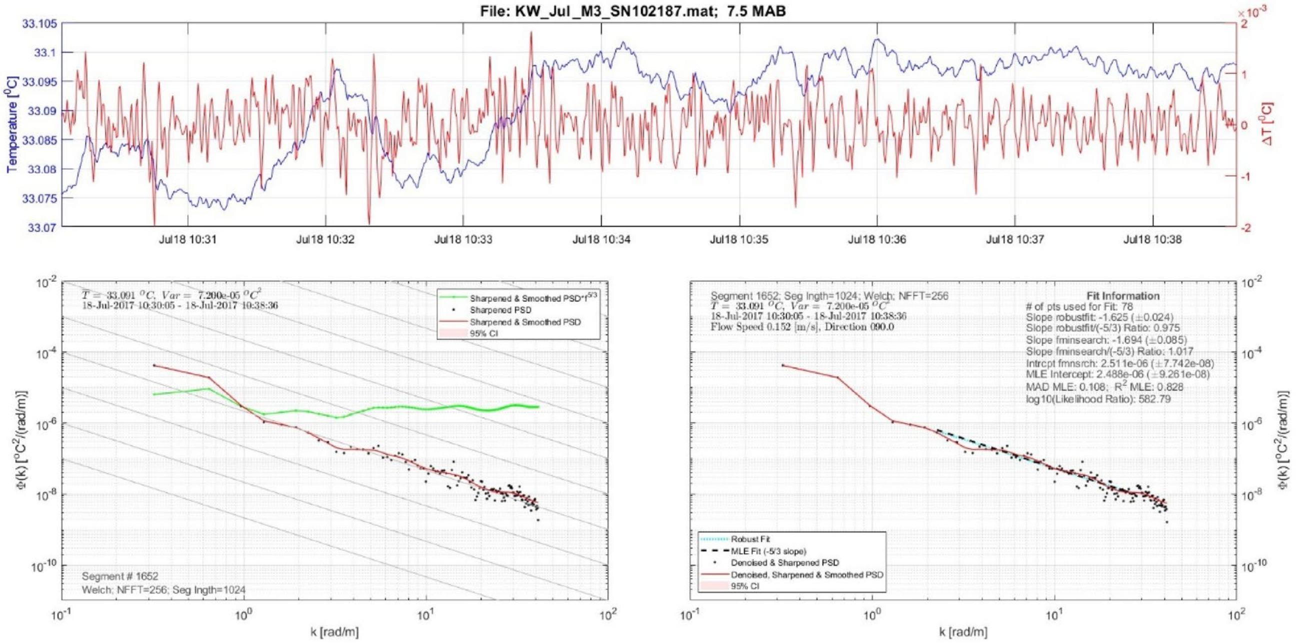

Fig. 8 PSD analysis and k-space fitting using the *solo_T_FitPSD_kSpace* function. The upper panel presents the time series of temperature (blue line) and its corresponding derivative (ΔT, red line) at 7.5 MAB. The lower left panel displays the temperature PSD in wavenumber space ($\Phi(k)$) derived from Welch's method with 1024-point segments. The green line represents the sharpened and smoothed PSD adjusted by a -5/3 slope, while the black dots depict the observed PSD. The red curve indicates the 95% confidence interval of the fitted PSD, which follows theoretical predictions for the inertial-convective range. The lower right panel shows the robust fit (dotted cyan line) and MLE fit (dashed black line) of the PSD in wavenumber space, with the denoised and smoothed PSD overlaid. Fit parameters such as slope, intercept, and log-likelihood are summarized on the panel for validation

and spectral analysis. The noise correction is achieved by predefined noise models produced earlier using the solo_*T_noise_spc* function and a specific sensor's bench test. This correction ensures that subsequent spectral calculations accurately represent the turbulent temperature fluctuations. Finally, the *solo_T_quick_calc* generates estimates and statistics of ϵ and χ_T for each segment, allowing to compare results across multiple datasets.

4 Comparison of RBR*solo*^{3} T Sensors and Turbulence Profilers Estimate of Turbulent Kinetic Energy Dissipation (ϵ) and Temperature Dissipation (χ_T) Rates

In this section, we assess the efficacy of this new method using fast response temperature sensors to provide reliable measurements of marine turbulence properties, specifically estimates of ϵ and χ_T, under two distinct dynamical conditions: (1) the wind- and buoyancy-driven system occurred during the calm, pre-Shamal and Shamal periods discussed above (described in Sect. 2.2 and detailed in Al Senafi et al. 2025); (2) an internal-wave-driven environment from a previous field campaign in 2017 (described in Sect. 2.3 and detailed in Al Senafi and Anis 2020b). For this purpose, we used two different turbulence profilers as benchmarks: the RSI MicroCTD and PME SCAMP.

4.1 Wind and Buoyancy Driven Environment

Figure 9 compares turbulence measurements obtained from two independent approaches: fast-response temperature sensors (RBR*solo*^{3} T) and a traditional shear probe based MicroCTD profiler, used here as the benchmark. The focus is on two key turbulence quantities, ϵ and χ_T, evaluated during distinct atmospheric forcing regimes including calm, pre-Shamal, and Shamal periods.

The time series of ϵ in Fig. 9A shows that RBR*solo*^{3} T sensors capture temporal fluctuations in turbulence levels during the enhanced mixing associated with Shamal wind events that are consistent with the MircoCTD approach. At 24 MAB, both the RBR*solo*^{3} T and the MicroCTD estimates of ϵ are within the same order of magnitude, ranging from 10^{-6} to 10^{-4} W/kg during peak forcing. These results demonstrate the ability of fast temperature sensors to resolve dynamic shifts in mixing intensity driven by both wind stress and buoyancy forcing. Furthermore, the histograms in Fig. 9C, which summarize the distribution of ϵ values across depths and time, show that the RBRsolo^3 T sensors (represented by bars) and the MicroCTD values (shown as lines)

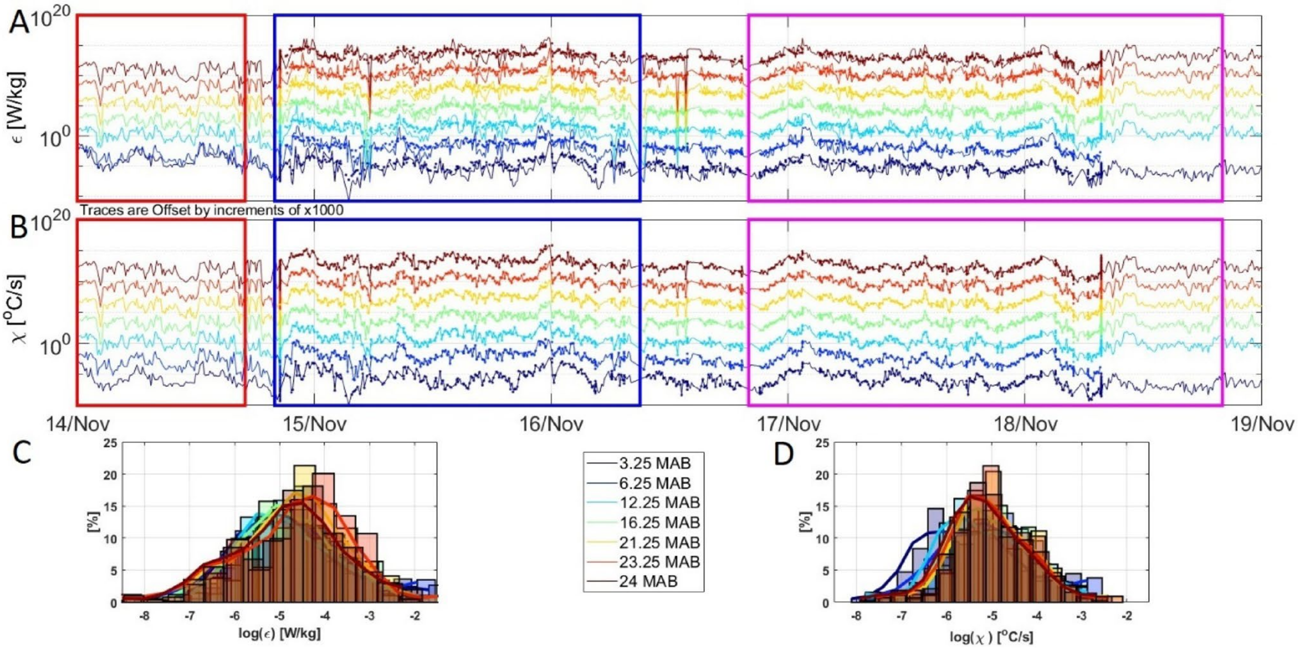

Fig. 9 Comparison of time-series data from seven fast-response (16 Hz) temperature sensors used to estimate (A) ϵ and (B) χ_T, with shallow sensors represented in warmer colors and deeper sensors in cooler colors. MicroCTD-derived estimates at the nearest measurement points are overlaid as dots. (C) and (D) display histograms illustrating the distribution of ϵ and χ_T estimates over the observation period. Red, blue, and magenta boxes indicate different atmospheric conditions: calm, pre-Shamal, and Shamal periods, respectively. MicroCTD profiling began late on November 14 and continued through the Shamal event, concluding midday on November 18, with no profiles collected during the calm period (Al Senafi et al. 2025)

produce similar distributions, particularly under strong wind forcing. RBR*solo*³ T sensors (represented by bars) and MicroCTD values (shown as lines) produce similar distributions, especially under strong wind forcing. Shallow sensors report elevated ϵ levels, averaging ~ 10^{-5} W/kg, consistent with the presence of wind-driven turbulence, while deeper sensors yield lower values closer to 10^{-6} W/kg. The average deviation between the two methods across all depths and periods remains within 2–10%. At 24 MAB, during the Shamal, the RBR*solo*³ T sensor estimated an average ϵ of 3.1×10^{-5} W/kg, closely matching the MicroCTD estimate of 3.5×10^{-5} W/kg.

The time series of χ_T shown in Fig. 9B obtained from RBR*solo*³ T sensors follow those from the MicroCTD through the different forcing phases. For example, during the Shamal, χ_T at 24 MAB ranged between 10^{-7} and 10^{-5} °C²/s across both approaches. Calm periods were associated with suppressed dissipation, with values remaining near ~ 10^{-7} °C²/s, indicative of reduced vertical mixing. Histograms of χ_T (Fig. 9D) support these trends, showing overlapping distributions between the two methods. Shallow sensors again exhibited the highest dissipation rates, while deeper sensors captured the increasingly suppressed mixing at depth. Differences between the two methods for χ_T were within 11–18%. For instance, at 12.25 MAB during the Shamal, χ_T from RBR*solo*³ T was approximately 2×10^{-6} °C²/s, closely mirroring the MicroCTD result.

In addition to temporal and statistical comparisons described above, the agreement between the two methodologies is further evaluated using scatter plots and Taylor diagrams (Fig. 10). The scatter plots display ϵ estimates from both approaches across seven depths, showing points clustering around the 1:1 line, indicating close agreement. While deviations increase with depth, suggesting increase in the influence of stratification and boundary layer turbulence. Correlation coefficients range from 0.49 to 0.66, indicating significant agreement, with the highest correlations observed near the seabed at 3.25 and 6.25 MAB, and the lowest near the surface at 23.25 and 24 MAB. The depth-dependent reduction in correlation is consistent with enhanced stratification and boundary-layer structure identified in Part I (Al Senafi et al. 2025), which suppress vertical motions and reduce the coherence between fixed-depth temperature-based estimates and profiler measurements at depth. The standard deviation values highlight that RBR*solo*³ T estimates exhibit greater variability compared to the MicroCTD at certain depths, particularly near the surface and seabed, where boundary layer effects may enhance turbulence. The standard deviation values are 1.01×10^{-5} W/kg near the surface to 0.82×10^{-5} W/kg near the seabed, with

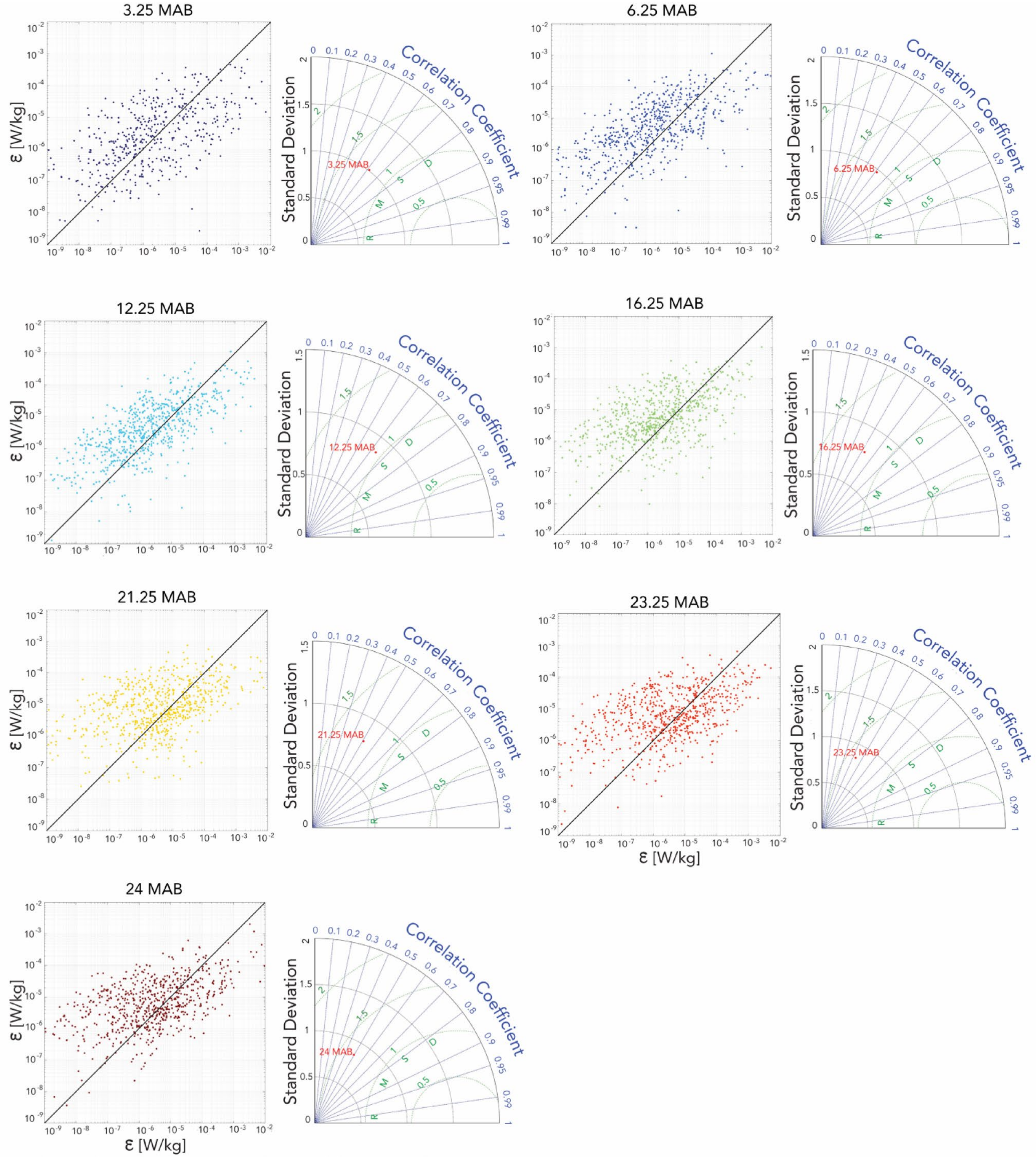

Fig. 10 Comparison of ϵ estimates from RBR*solo*^{3} T method and MicroCTD method at different depths during the 2023 field campaign. (Left panels): Scatter plots at seven depths (3.25, 6.25, 12.25, 16.25, 21.25, 23.25, and 24 MAB), with color coding corresponding to depth as in Fig. 8. The black 1:1 line represents perfect agreement. (Right panels): Taylor diagrams summarizing statistical agreement at each depth. Each point represents a different depth, showing correlation coefficient, standard deviation, and Root Mean Square Difference (RMSD) between the two methods. Note: RMSD and standard deviations were scaled by a factor of 1000 for improved visualization

intermediate depths showing lower values of 0.79×10^{-5} W/kg and 0.80×10^{-5} W/kg.

Despite minor discrepancies, the Root Mean Square Difference (RMSD) remains within an acceptable range, with values below 1.37×10^{-5} W/kg, emphasizing the reliability of RBR*solo*³ T sensors as a cost-effective alternative to traditional shear-probe profiler measurements for estimating turbulence dissipation in dynamic coastal environments.

4.2 Internal Wave Driven Conditions

In this section, we present a snapshot of a midsummer 2017 field campaign conducted off the coast of Kuwait, in the northern Gulf. During this campaign, continuous turbulence profiling was carried out using the MicroCTD and SCAMP turbulence profiler, and multiple moorings equipped with fast-response RBR*solo*³ T sensors to capture internal waves across and along the Kuwait coastline (for details of the field campaign see Al Senafi and Anis 2020b; 2020c). While internal waves introduce non-stationarity at larger scales, the turbulence estimates are derived from inertial–convective scales that are well separated from the internal wave band (Al Senafi and Anis 2020b; 2020c), enabling robust estimation of ϵ and χ_T.

Examination of Figs. 11A (ϵ) and 11B (χ_T) shows close agreement between the turbulent quantities estimated from the RBR*solo*³ T sensors and the microstructure profilers, with the estimates of the proposed method (blue traces) closely tracking those of MicroCTD (gray and black crosses) and SCAMP (red asterisks) across time. The comparison is shown for a distance from the bottom of 7.5 m. We recall that the RBR*solo*³ T sensors were moored, providing continuous data, while the MicroCTD and SCAMP profilers captured vertical profiles at a rate of one profile every 5–6 min, approximately. Despite this difference in approach, both methods reveal similar turbulence patterns. During turbulent periods of peak internal wave activity (e.g., around 6:00, 9:00, and 15:00), the RBR*solo*³ T estimates align well with the MicroCTD and SCAMP data, indicating that the RBR*solo*³ T sensors effectively capture the dynamic changes in turbulent energy. The average ϵ value from the RBR*solo*³ T sensors was 3.52×10^{-8} W/kg, that of MicroCTD was 5.57×10^{-8} W/kg and 6.11×10^{-8} W/kg for the two shear probes, and that of SCAMP was 4.38×10^{-8} W/kg (Table 12 A). The ϵ estimates were closely aligned with a margin of error of 1–3%. The average χ_T value from the RBR*solo*³ T sensors was 2.4×10^{-9} °C²/s, and that from SCAMP was 1.11×10^{-9} °C²/s (Table 12B). As for the MicroCTD data, we reported some problems with the FP07 and the precise conductivity-temperature sensor during the deployment, probably because the profiler hit the bottom during the previous day. The estimates of χ_T may therefore be biased even though they passed the quality metrics, as appears to be the case when analyzing Fig. 11B. In

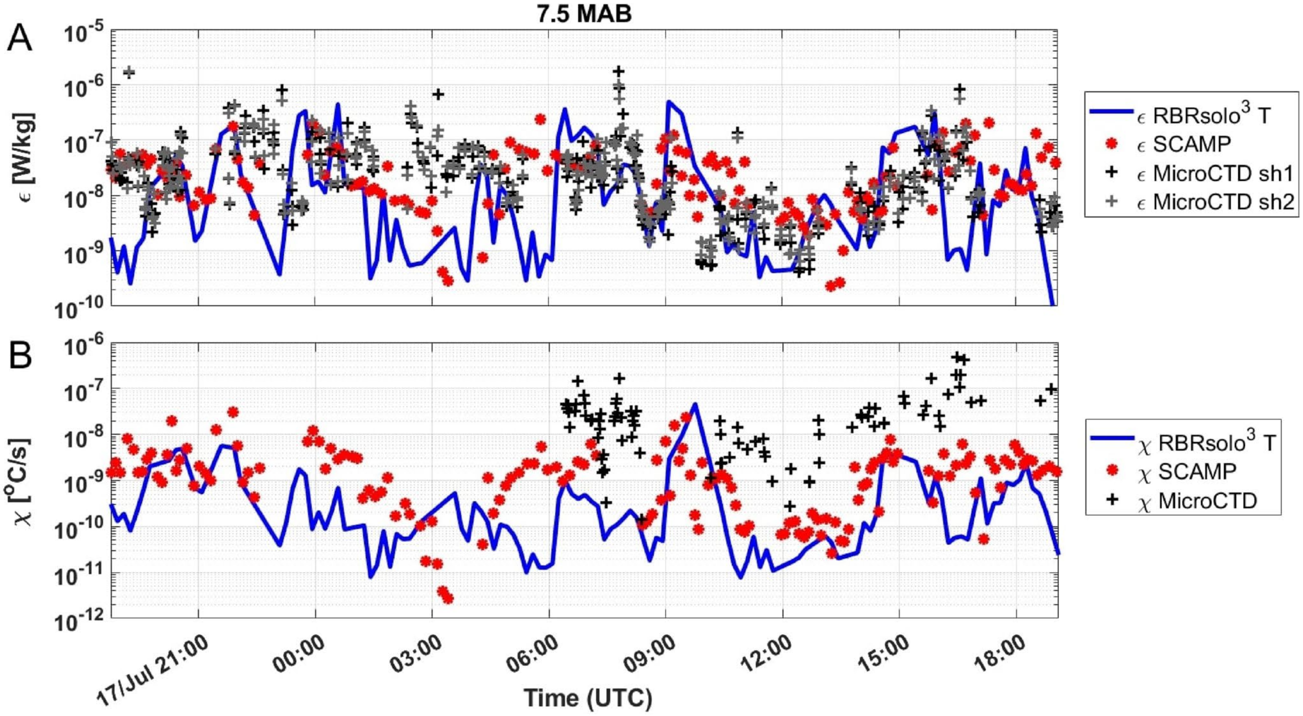

Fig. 11 Comparison of time series of (**A**) ϵ estimated from moored RBR*solo*³ T (blue), MicroCTD (gray and black), and SCAMP (red); (**B**) χ_T estimated from moored RBR*solo*³ T (blue), MicroCTD (black), and SCAMP (red) during 17 and 18 July 2017. The data refers to 7.5 MAB. We note that the χ_T estimates from the MicroCTD are biased most probably because the instrument hit the bottom (see Sect. 3.4.2)

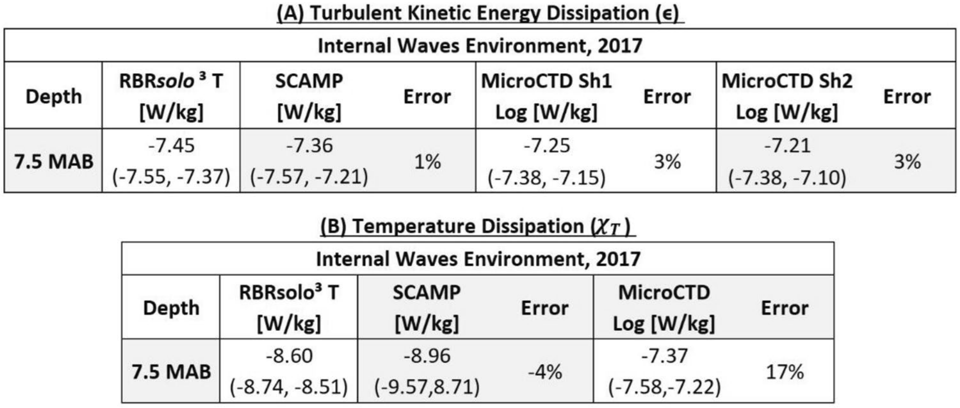

(A) Turbulent Kinetic Energy Dissipation (ϵ)

Internal Waves Environment, 2017							
Depth	RBR*solo*³ T [W/kg]	SCAMP [W/kg]	Error	MicroCTD Sh1 Log [W/kg]	Error	MicroCTD Sh2 Log [W/kg]	Error
7.5 MAB	-7.45 (-7.55, -7.37)	-7.36 (-7.57, -7.21)	1%	-7.25 (-7.38, -7.15)	3%	-7.21 (-7.38, -7.10)	3%

(B) Temperature Dissipation (χ_T)

Internal Waves Environment, 2017					
Depth	RBRsolo³ T [W/kg]	SCAMP [W/kg]	Error	MicroCTD Log [W/kg]	Error
7.5 MAB	-8.60 (-8.74, -8.51)	-8.96 (-9.57,8.71)	-4%	-7.37 (-7.58,-7.22)	17%

Fig. 12 Comparison of Turbulent Kinetic Energy Dissipation (ϵ) and Temperature Dissipation (χ_T) estimates from RBR*solo*³ T sensors and our benchmark profilers (MicroCTD and SCAMP). (**A**) ϵ estimates (log scale), (**B**) χ_T estimates (log scale). The tables display averages and 95% confidence intervals (in parentheses) for RBR*solo*³ T and MicroCTD at 7.5 MAB depth during the 2017 internal waves conditions. A total of 1467 points were used for the statistical analysis. Error percentage indicates the difference between RBR*solo*³ T and the benchmark profiler.

this figure we reported only part of the data after filtering out those that were clearly associated with noisy temperature microstructure data (i.e., before 6 am on 18 July). The overall trend is consistent with that of RBR*solo*³ T and SCAMP, but biased towards higher values, averaging 4.28×10^{-8} °C²/s (Table 12B). While microstructure data are more reliable, the instruments used to collect them are delicate and the results presented here clearly highlight the robustness of the proposed procedure as one of its key advantages, along with its ability to allow for continuous measurements.

Based on our results from comparison of turbulence parameters during periods of different physical forcings (wind stress, convection, internal waves) we suggest that moored, temperature sensors may provide an inexpensive, reliable, and robust alternative to traditional turbulence profiling for estimation of ϵ and χ_T time series.

5 Conclusions

This study introduces the *SOLO_T* Toolbox, a purpose-built MATLAB framework designed to estimate turbulent parameters (ϵ and χ_T) from high-resolution temperature time-series. The toolbox provides a practical and cost-effective approach for deriving turbulence estimates from affordable fast-response thermistors, offering a complementary option to traditional turbulence measurement systems rather than a replacement.

Through comprehensive validation against two microstructure profilers (RSI MicroCTD and PME SCAMP), we demonstrated that the *SOLO_T* Toolbox produces consistent and physically meaningful estimates across a range of dynamical regimes, including wind-driven mixing, convective forcing, and internal wave activity. Deviations between *SOLO_T* based estimates and benchmark measurements remained within 2–10% for ϵ and 11–18% for χ_T, while RMSD values were consistently below 1.37×10^{-5} W/kg. Correlation coefficients for ϵ ranged from 0.49 to 0.66, highlighting the method's capacity to capture turbulence variability across depth and time.

The strength of the *SOLO_T* Toolbox lies in its integration of theoretical turbulence models, spectral analysis techniques, and practical deployment configurations into an accessible, user-friendly package. By eliminating the need for expensive shear probes or complex profiler systems, this toolbox lowers the barrier to high-frequency turbulence measurements, especially in coastal and semi-enclosed seas where operational constraints are common. The release of this toolbox, along with detailed documentation and example datasets, is intended to support its adoption by the wider atmospheric, oceanographic and environmental communities. It enables reproducible, long-duration, and spatially distributed turbulence observations that are otherwise challenging with conventional instrumentation.

Future work will focus on expanding the toolbox's functionality to estimate additional mixing parameters, including vertical diffusivities of salinity and momentum, and on incorporating adaptive, data-driven quality-control procedures to further improve robustness across a wider range of flow regimes. Extensions to multi-sensor configurations and the integration of complementary observations (e.g., velocity or density measurements where available) will also be explored to improve estimates of stratification and mixing efficiency. These developments will enable the use of

Solo_T–derived diffusivities to investigate the impacts of episodic atmospheric forcing, including Shamal winds and rainfall events, on vertical mixing and ecosystem processes in shallow and semi-enclosed systems such as the Arabian Gulf. Overall, the *Solo_T* Toolbox represents a step toward enabling sustained, cost-effective observations of small-scale turbulence and mixing, with potential applications across a broad range of coastal, semi-enclosed, and open-ocean environments.

Acknowledgements We thank the Kuwaiti Coast Guard for providing field logistics, transportation and divers. We also thank the undergraduate students from the Marine Science Department at Kuwait University for their invaluable assistance in the field. Special thanks are extended to Mr. Yusuf Bohadi, Mr. Abdulhadi Esmail, and Mr. Mostafa Omar for their dedicated contributions in the field. Additionally, we are grateful to Ms. Noor Al Fayez for her expertise in the schematic design of the experimental setup. We also thank Dr. Hala Al Jassar from the Physics Department at Kuwait University for providing access to satellite imagery. The KuwaitSat-1 image used in the graphical abstract was obtained through Project #FP-18-14-SP-01, which was supported by funding from the KFAS.

Author Contributions Fahad Al Senafi: Writing – original draft, review & editing, Project administration, Supervision, Methodology, Investigation, Formal analysis, Visualization, Conceptualization, Funding acquisition. Ayal Anis: Writing – review & editing, Methodology, Formal analysis, Conceptualization. Tariq Al Rushaid: Writing – review & editing, Formal analysis, Investigation, Funding acquisition. Sebastiano Piccolroaz: Writing – review & editing, Methodology, Formal analysis.

Funding This project was funded by both Kuwait Foundation for the Advancement of Sciences (KFAS) under project code: CN21-44SE-1369 and the Research Sector at Kuwait University (KU) under project code: RX-01/21.

Data Availability All data used in this study, including temperature time-series from the RBR sensors, ADCP velocity profiles, and processed turbulence estimates, are available upon request.

Declarations

Competing Interests The authors declare that they have no known competing financial interests or personal relationships that could have appeared to influence the work reported in this paper.

References

Al Senafi F, Anis A (2020b) Internal waves on the continental shelf of the Northwestern Arabian Gulf. Front Mar Sci 6:1–19. https://doi.org/10.3389/fmars.2019.00804

Al Senafi F, Anis A, Estuarine (2020a) Coastal Shelf Sci, 233, 106511

Al Senafi FA, Abed RMM, Muthukrishnan T, Anis A, Mahmoud H (2020c) Development and diversity of bacterial biofilms in response to internal tides: A case study off the coast of Kuwait. Front Mar Sci 7:1–13. https://doi.org/10.3389/fmars.2020.00107

Al Senafi F, Anis A, Rushaid A, Piccolroaz T (2025) P. A Novel Cost-Effective Approach for Collecting Time-Series of Turbulence Properties in Aquatic Systems, Earth Systems and Environment (in press)

Alif HA, Mashrafi MJ, Elhag M et al (2025a) (). Artificial Intelligence-Driven Rainfall Forecasting and GIS-Based Flood Risk Mapping for Climate-Resilient Infrastructure in Bangladesh.). Artificial Intelligence-Driven Rainfall Forecasting and GIS-Based Flood Risk Mapping for Climate-Resilient Infrastructure in Bangladesh. Earth Syst Environ (2025). https://doi.org/10.1007/s41748-025-00958-8

Alif HA, Mashrafi MJ, Haldar U et al (2025b) Machine Learning-Driven Rainfall Forecasting Model for Sustainable and Adaptive Infrastructure Planning. https://doi.org/10.21203/rs.3.rs-7109251/v1

Anis A, Singhal G (2006) Mixing in the surface boundary layer of a tropical freshwater reservoir. J Mar Syst 63:225–243

Bakun A, Black BA, Bograd SJ et al (2015) Anticipated Effects of Climate Change on Coastal Upwelling Ecosystems. Curr Clim Change Rep 1:85–93. https://doi.org/10.1007/s40641-015-0008-4

Batchelor GK (1959) Small-scale variation of convected quantities like temperature in turbulent fluid: Part 1. General discussion and the case of small conductivity. J Fluid Mech 5:113–133. https://doi.org/10.1017/S002211205900009X

Bruciaferri D, Tonani M, Ascione I, Al Senafi F, O'Dea E, Hewitt HT, Saulter A (2022) GULF18, a high-resolution NEMO-based tidal ocean model of the Arabian/Persian Gulf, Geosci. Model Dev 15:8705–8730

Danaila L, Antonia RA (2009) Spectrum of a passive scalar in moderate Reynolds number homogeneous isotropic turbulence. Phys Fluids 21(11):111702. https://doi.org/10.1063/1.3253819

Emery WJ, Thomson RE (2004) Data Analysis Methods in Physical Oceanography, 2nd edn. Elsevier, Amsterdam

Fieseler C, Al-Mudaffar N, Helmuth B, Leitão A, Al-Ainsi M, Al Mukaimi M, Al-Saidi M, Senafi A, Bejarano F, Ben-Hamadou I, D'Addario R, Dheen J, Giraldes M, Glowka B, Johnson L, Lyons M, Mateos-Molina B, Marshall D, Mohammed C, Range S, Shokri P, Wong M, J., Pyenson N (2023) Expanding ocean protection and peace: a window for science diplomacy in the Gulf. R Soc Open Sci 10:230392

Ghosh H, Rahat IS, Emon MMR et al (2025) Advanced neural network architectures for tomato leaf disease diagnosis in precision agriculture. Discov Sustain 6:312. https://doi.org/10.1007/s43621-025-01149-1

Gregg MC, Meagher TB (1980) The dynamic response of glass rod thermistors. J Geophys Res 85(C5):2779–2786. https://doi.org/10.1029/JC085iC05p02779

Harris FJ (1978) On the Use of Windows for Harmonic Analysis with the Discrete Fourier Transform. Proceedings of the IEEE. Vol. 66, pp. 51–83

Hayes MH (1996) Statistical Digital Signal Processing and Modeling. Wiley, New York

Hill RJ (1978) Models of the scalar spectrum for turbulent advection. J Fluid Mech 88(3):541–562. https://doi.org/10.1017/S002211207800227X

Hummersone C (2024) IoSR Matlab Toolbox: Toolbox for MATLAB Software, Institute of Sound Recording, University of Surrey. Available from: https://github.com/IoSR-Surrey/MatlabToolbox

I Taylor G (1938) The spectrum of turbulence. Proc R Soc Lond A 164(919):476–490

Ivey G, Winters K, Koseff J (2008) Density Stratification, Turbulence, but How Much Mixing? Annual Rev Fluid Mech 40:169–184. https://doi.org/10.1146/annurev.fluid.39.050905.110314

Kerr RM (1990) Velocity, scalar and transfer spectra in numerical turbulence. J Fluid Mech 211:309–332. https://doi.org/10.1017/S0022112090001586

Kraichnan R (1968) Small-scale structure of a scalar field convected by turbulence. Phys Fluids 11(5):945–953. https://doi.org/10.1063/1.1692063

Kundu P, Cohen IM (2012) Fluid mechanics, 5th edn. Elsevier

Li D, Anis A, Al Senafi F (2020a) Physical Response of the Northern Arabian Gulf to Winter Shamals. J Mar Syst 203:103280

Li D, Anis A, Al Senafi F (2020b) Neap-Spring Variability of Tidal Dynamics in the Northern Arabian Gulf. Cont Shelf Res 197:104086

Mercier P, Thiébaut M, Guillou S, Maisondieu C, Poizot E, Pieterse A, Thiébot J, Filipot JF, Grondeau M (2021) Turbulence measurements: An assessment of acoustic Doppler current profiler accuracy in rough environment.Ocean Eng. 226:108819. https://doi.org/10.1016/j.oceaneng.2021.108819

Nash JD, Caldwell DR, Zelman MJ, Moum JN (1999) A Thermocouple Probe for High-Speed Temperature Measurement in the Ocean. J Atmos Ocean Technol 16:1474–1482. https://doi.org/10.1175/1520-0426(1999)016%3C1474:ATPFHS%3E2.0.CO;2

Oakey NS (1982) Determination of the rate of dissipation of turbulent energy from simultaneous temperature and velocity shear microstructure measurements. J Phys Oceanogr 12:256–271. https://doi.org/10.1175/1520-0485(1982)012

Oppenheim AV, Ronald W, Schafer JR, Buck (1999) Discrete-Time Signal Processing. Prentice Hall, Upper Saddle River, NJ

Osborn TR (1980) Estimates of the Local Rate of Vertical Diffusion from Dissipation Measurements. J Phys Oceanogr 10:83–89. https://doi.org/10.1175/1520-0485(1980)010%3C0083:EOTLRO%3E2.0.CO;2

Osborn TR, Cox CS (1972) Oceanic fine structure. Geophys Fluid Dynamics 3(4):321–345. https://doi.org/10.1080/03091927208236085

Piccolroaz S, Fernández-Castro B, Toffolon M et al (2021) A multisite, year-round turbulence microstructure atlas for the deep perialpine Lake Garda. Sci Data 8:188. https://doi.org/10.1038/s41597-021-00965-0

Portwood GD, de Bruyn Kops SM, Caulfield CP (2022) Implications of inertial subrange scaling for stably stratified mixing. J Fluid Mech 939:10. https://doi.org/10.1017/jfm.2022.160

Press WH, Flannery BP, Teukolsky SA, Vetterling WT (1992) Numerical Recipes in Fortran 77: The Art of Scientific Computing, 2nd edn. Cambridge University Press

Rockland Scientific (2022) MicroCTD User Manual (PN 010-150-20), Revision 1.1. Rockland Scientific

Ruddick B, Anis A, Thompson K (2000) Maximum likelihood spectral fitting: The Batchelor spectrum. J Atmos Ocean Technol 17(11):1541–1555. https://doi.org/10.1175/1520-0426(2000)017

Smith DL, Goodwin RA, Nestler JM (2014) Relating Turbulence and Fish Habitat: A New Approach for Management and Research. Reviews Fisheries Sci Aquaculture 22(2):123–130. https://doi.org/10.1080/10641262.2013.803516

Spingys CP, Williams RG, Tuerena RE, Garabato N, Vic A, Forryan C, A., Sharples J (2021) Observations of nutrient supply by mesoscale eddy stirring and small-scale turbulence in the oligotrophic North Atlantic. Glob Biogeochem Cycles, 35, 12, e2021GB007200. https://doi.org/10.1029/2021GB007200

Sreenivasan KR (1995) On the universality of the Kolmogorov constant. Phys Fluids 7(11):2778–2784. https://doi.org/10.1063/1.868656

Sreenivasan KR (1996) The passive scalar spectrum and the Obukhov-Corrsin constant. Phys Fluids 8(1):189–196. https://doi.org/10.1063/1.868768

St. Laurent L, Merrifield S (2017) Measurements of Near-Surface Turbulence and Mixing from Autonomous Ocean Gliders. Oceanography 30(2):116–125

Stevens C, Smith M, Ross A (1999) SCAMP: Measuring turbulence in estuaries, lakes and coastal waters. Water Atmos 7:20–21

Stoica P, Moses R (2005) Spectral Analysis of Signals. Prentice Hall, Upper Saddle River, NJ

Tagawa M, Kato K, Ohta Y (2003) Response compensation of thermistors: Frequency response and identification of thermal time constant. Rev Sci Instrum 74(3):1350–1358. https://doi.org/10.1063/1.1542668

Thomson J, Talbert J, De Klerk A, Zippel S, Guerra M, Kilcher L (2015) Turbulence measurements from moving platforms, IEEE/OES Eleveth Current, Waves and Turbulence Measurement (CWTM), St. Petersburg, FL, USA, 2015, pp. 1–5. https://doi.org/10.1109/CWTM.2015.7098107

Tozzi S, Schofield O, Falkowski P (2004) Historical climate change and ocean turbulence as selective agents for two key phytoplankton functional groups. Mar Ecol Prog Ser 274:123–132. https://doi.org/10.3354/meps274123

Wang LH, Zhang WY, Hao X et al (2020) Surface wave effects on energy transfer in overlying turbulent flow. J Fluid Mech 893:A21. https://doi.org/10.1017/jfm.2020.246

Welch PD (1967) The Use of the Fast Fourier Transform for the Estimation of Power Spectra: A Method Based on Time Averaging Over Short, Modified Periodograms. IEEE Trans Audio Electroacoust AU–15:70–73

Wilczek M, Xu H, Narita Y (2014) A note on Taylor's hypothesis under large-scale flow variation. Nonlin Processes Geophys 21:645–649. https://doi.org/10.5194/npg-21-645-2014